An efficient transient Navier–Stokes solver on compact nonuniform space grids

Article *in* Journal of Computational and Applied Mathematics · April 2008

DOI: 10.1016/j.cam.2007.02.021

CITATIONS
30

READS
505

3 authors, including:

Jiten C. Kalita
Indian Institute of Technology Guwahati
74 PUBLICATIONS **1,220** CITATIONS
SEE PROFILE

Nimisha Nidhi
Indian Institute of Technology Guwahati
1 PUBLICATION **30** CITATIONS
SEE PROFILE

Available online at www.sciencedirect.com
ScienceDirect
Journal of Computational and Applied Mathematics 214 (2008) 148–162
JOURNAL OF COMPUTATIONAL AND APPLIED MATHEMATICS
www.elsevier.com/locate/cam

An efficient transient Navier–Stokes solver on compact nonuniform space grids

Jiten C. Kalita[a,*], Anoop K. Dass[b], Nimisha Nidhi[b]

[a] *Department of Mathematics, Indian Institute of Technology Guwahati, 781039, India*
[b] *Department of Mechanical Engineering, Indian Institute of Technology Guwahati, 781039, India*

Received 16 August 2006; received in revised form 10 February 2007

Abstract

In this paper, we propose an implicit higher-order compact (HOC) finite difference scheme for solving the two-dimensional (2D) unsteady Navier–Stokes (N–S) equations on nonuniform space grids. This temporally second-order accurate scheme which requires no transformation from the physical to the computational plane is at least third-order accurate in space, which has been demonstrated with numerical experiments. It efficiently captures both transient and steady-state solutions of the N–S equations with Dirichlet as well as Neumann boundary conditions. The proposed scheme is likely to be very useful for the computation of transient viscous flows involving free and wall bounded shear layers which invariably contain spatial scale variation. Numerical results are presented and compared with analytical as well as established numerical data. Excellent comparison is obtained in all the cases.

Keywords: Transient; HOC; Navier–Stokes equations; Nonuniform; High accuracy; Finite differences

1. Introduction

The unsteady 2D incompressible Navier–Stokes (N–S) equations in the traditional primitive variable formulation in nondimensional form can be written as

$$\frac{\partial u}{\partial x} + \frac{\partial v}{\partial y} = 0, \tag{1}$$

$$\frac{\partial u}{\partial t} + u\frac{\partial u}{\partial x} + v\frac{\partial u}{\partial y} = -\frac{\partial p}{\partial x} + \frac{1}{Re}\nabla^2 u, \tag{2}$$

$$\frac{\partial v}{\partial t} + u\frac{\partial v}{\partial x} + v\frac{\partial v}{\partial y} = -\frac{\partial p}{\partial y} + \frac{1}{Re}\nabla^2 v. \tag{3}$$

Here u and v are the velocities along the x- and y-directions, t is the time, Re is the Reynolds number and p is the pressure. Though this formulation accurately represents the fluid flow phenomena, its direct solution is normally difficult to obtain due to the pressure term in Eqs. (2) and (3). Partly in order to avoid handling the pressure variable, an

* Corresponding author. Tel.: +91 361 2582 614; fax: +91 361 2690 762.
E-mail addresses: jiten@iitg.ernet.in (J.C. Kalita), anoop@iitg.ernet.in (A.K. Dass), Nimisha.Nidhi@gmail.com (N. Nidhi).

0377-0427/$ - see front matter © 2007 Elsevier B.V. All rights reserved.
doi:10.1016/j.cam.2007.02.021

alternative formulation using streamfunction ψ and vorticity ω has been used for several decades. The ψ–ω formulation can be written as

$$\omega_t - \frac{1}{Re}(\omega_{xx} + \omega_{yy}) + (u\omega_x + v\omega_y) = 0, \tag{4}$$

$$\psi_{xx} + \psi_{yy} = -\omega(x, y), \tag{5}$$

with

$$u = \psi_y, \quad v = -\psi_x \quad \text{and} \quad \omega = u_y - v_x. \tag{6}$$

Various schemes [1,4–7,11,14,15,17,21,23,29] have been proposed in the near past to solve the N–S equations both in the primitive variable (Eqs. (1)–(3)) and the ψ–ω (Eqs. (4)–(6)) form. Amongst these, Eqs. (2)–(4) are of convection–diffusion type. Of late, the higher-order compact (HOC) finite-difference schemes [3,8–10,12–15,18–20,25,26] for the computation of flows of this type, particularly incompressible viscous flows governed by the N–S equations, are gradually gaining popularity because of their high accuracy and advantages associated with compact difference stencils. A compact finite difference scheme is one which utilizes grid points located only directly adjacent to the node about which the differences are taken. In addition, if the scheme has an order of accuracy greater than two, it is termed a higher-order compact method. The higher-order accuracy of the HOC methods combined with the compactness of the difference stencils yields highly accurate numerical solutions on relatively coarser grids with greater computational efficiency. However, most of the HOC formulations [8,9,13,15,19,20,25] have been carried out only for the steady-state form of the N–S equations. Whenever there has been attempts to develop HOC schemes for transient N–S equations, they are confined mostly to uniform space grid only [3,12,14,18,26].

In the present paper, we propose an HOC scheme for the transient N–S equation on nonuniform space grids. The scheme is implicit, second-order time-accurate and the space accuracy is three or four depending on the pattern of grid spacing. The scheme which is developed for the transient 2D convection–diffusion equations with variable coefficients can easily be accommodated into equations of N–S type with slight adjustment of the convection coefficients. It handles both Dirichlet and Neumann boundary conditions with ease. To validate the scheme, it is first applied to a transient problem having analytical solution, namely the Taylor vortex problem and then to the lid-driven square cavity problem where steady state is arrived at in a time-marching fashion. Our results are compared with analytical and well-established numerical results, and excellent match is obtained in all the cases.

The paper is organized in the following way: Section 2 deals with the basic formulation and numerical procedures, Section 3 with numerical experiments and finally Section 4, the conclusions.

2. Basic formulations and numerical procedures

The unsteady convection–diffusion equation in 2D for a flow variable ϕ can be written as

$$b\frac{\partial \phi}{\partial t} - \nabla^2\phi + c(x, y, t)\frac{\partial \phi}{\partial x} + d(x, y, t)\frac{\partial \phi}{\partial y} = f(x, y, t), \tag{7}$$

where $b > 0$ is a constant, c and d are convection coefficients in the x- and y-directions, respectively, and f is a forcing function. Recently, we have developed a transformation-free higher-order compact scheme on nonuniform grids [2] for the steady-state form

$$-\nabla^2\phi + c(x, y)\frac{\partial \phi}{\partial x} + d(x, y)\frac{\partial \phi}{\partial y} = f(x, y), \tag{8}$$

of Eq. (7). The scheme on rectangular Cartesian coordinate system does not require any transformation from the physical plane to the computational plane. On a grid point (i, j) in the computational domain (the stencil is similar to the one at the n or $(n + 1)$th time level shown in Fig. 1), the scheme for Eq. (8) is given by

$$[-A_{ij}\delta_x^2 - B_{ij}\delta_y^2 + C_{ij}\delta_x + D_{ij}\delta_y + G_{ij}\delta_x\delta_y - H_{ij}\delta_x\delta_y^2 - K_{ij}\delta_x^2\delta_y - L_{ij}\delta_x^2\delta_y^2]\phi_{ij} = F_{ij}, \tag{9}$$

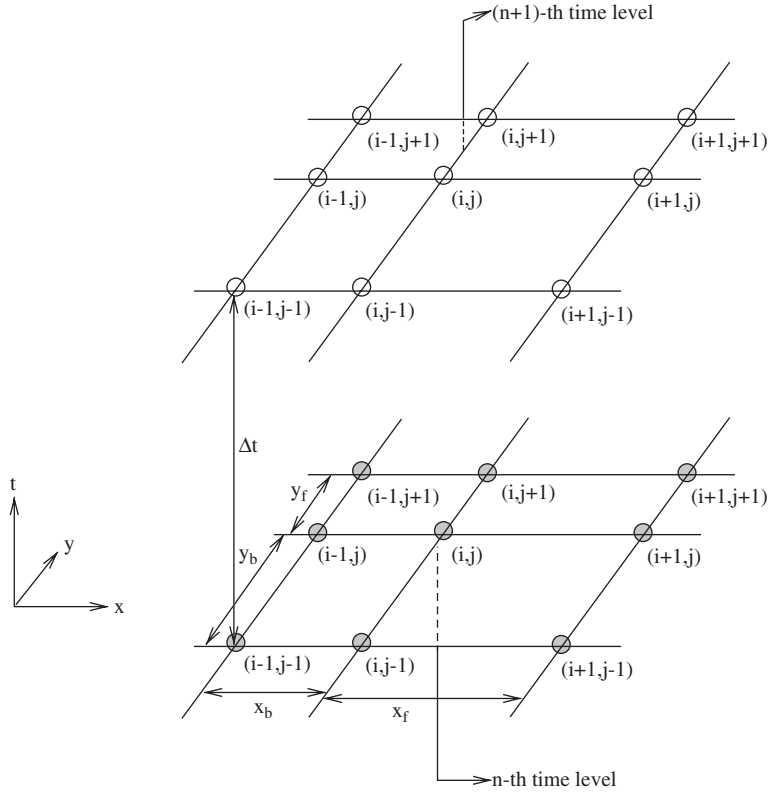

Fig. 1. The (9, 9) higher-order compact stencil on nonuniform grid in *xyt*-space.

where the coefficients C_{ij}, D_{ij}, A_{ij} ,B_{ij}, G_{ij}, H_{ij}, K_{ij}, L_{ij} and F_{ij} are given by

$$C_{ij} = [1 + (H_1 + H_2c)\delta_x + (K_1 + K_2d)\delta_y + \{H_2 - 0.5(x_f - x_b)(H_1 + H_2c)\}\delta_x^2 + \{K_2 - 0.5(y_f - y_b)(K_1 + K_2d)\}\delta_y^2]c, \tag{10}$$

$$D_{ij} = [1 + (H_1 + H_2c)\delta_x + (K_1 + K_2d)\delta_y + \{H_2 - 0.5(x_f - x_b)(H_1 + H_2c)\}\delta_x^2 + \{K_2 - 0.5(y_f - y_b)(K_1 + K_2d)\}\delta_y^2]d, \tag{11}$$

$$A_{ij} = 1 - [(H_1 + H_2c) + 2H_2\{\delta_x c - 0.5(x_f - x_b)\delta_x^2 c\}] + 0.5(x_f - x_b)C_{ij}, \tag{12}$$

$$B_{ij} = 1 - [(K_1 + K_2d) + 2K_2\{\delta_y d - 0.5(y_f - y_b)\delta_y^2 d\}] + 0.5(y_f - y_b)D_{ij}, \tag{13}$$

$$G_{ij} = (H_1 + H_2c)d + (K_1 + K_2d)c + 2H_2\delta_x d + 2K_2\delta_y c - \{H_2(x_f - x_b)\delta_x^2 d + K_2(y_f - y_b)\delta_y^2 c\}, \tag{14}$$

$$H_{ij} = H_1 + H_2c - K_2c, \tag{15}$$

$$K_{ij} = K_1 + K_2d - H_2d, \tag{16}$$

$$L_{ij} = H_2 + K_2 \tag{17}$$

and

$$F_{ij} = [1 + (H_1 + H_2c)\delta_x + (K_1 + K_2d)\delta_y + \{H_2 - 0.5(x_f - x_b)(H_1 + H_2c)\}\delta_x^2 + \{K_2 - 0.5(y_f - y_b)(K_1 + K_2d)\}\delta_y^2]f_{ij}, \tag{18}$$

with

$$H_1 = \tfrac{1}{6}\{2(x_\mathrm{f} - x_\mathrm{b}) - cx_\mathrm{f}x_\mathrm{b}\}, \quad H_2 = \tfrac{1}{24}\{2(x_\mathrm{f}^2 + x_\mathrm{b}^2 - x_\mathrm{f}x_\mathrm{b}) - cx_\mathrm{f}x_\mathrm{b}(x_\mathrm{f} - x_\mathrm{b})\}$$

and

$$K_1 = \tfrac{1}{6}\{2(y_\mathrm{f} - y_\mathrm{b}) - dy_\mathrm{f}y_\mathrm{b}\}, \quad K_2 = \tfrac{1}{24}\{2(y_\mathrm{f}^2 + y_\mathrm{b}^2 - y_\mathrm{f}y_\mathrm{b}) - dy_\mathrm{f}y_\mathrm{b}(y_\mathrm{f} - y_\mathrm{b})\}.$$

Here, x_f, x_b are the forward and the backward step lengths in the x-direction given by $x_\mathrm{f} = x_{i+1,j} - x_{i,j}$ and $x_\mathrm{b} = x_{i,j} - x_{i-1,j}$, and y_f, y_b represent the same in the y-direction. The details of the finite difference operators δ_x, δ_y, δ_x^2, δ_y^2, $\delta_x\delta_y$, $\delta_x\delta_y^2$, $\delta_x^2\delta_y$ and $\delta_x^2\delta_y^2$ can be found in the appendix.

To derive a finite difference scheme for the unsteady Eq. (7) we replace the forcing function f in Eq. (8) by $f - b(\partial\phi/\partial t)$. Thus the term f_{ij} in Eq. (18) is replaced by $f_{ij} - b(\partial\phi/\partial t)|_{ij}$. We then approximate the time derivative term with forward difference whence Eq. (9) yields

$$\begin{aligned}
&[-A_{ij}\delta_x^2 - B_{ij}\delta_y^2 + C_{ij}\delta_x + D_{ij}\delta_y + G_{ij}\delta_x\delta_y - H_{ij}\delta_x\delta_y^2 - K_{ij}\delta_x^2\delta_y - L_{ij}\delta_x^2\delta_y^2]\phi_{ij}^n \\
&\quad = [1 + (H_1 + H_2c)\delta_x + (K_1 + K_2d)\delta_y + \{H_2 - 0.5(x_\mathrm{f} - x_\mathrm{b})(H_1 + H_2c)\}\delta_x^2 \\
&\qquad + \{K_2 - 0.5(y_\mathrm{f} - y_\mathrm{b})(K_1 + K_2d)\}\delta_y^2](f_{ij} - b\delta_t^+\phi_{ij}^n),
\end{aligned}$$

which can be written finally as

$$\begin{aligned}
&b[1 + (H_1 + H_2c)\delta_x + (K_1 + K_2d)\delta_y + \{H_2 - 0.5(x_\mathrm{f} - x_\mathrm{b})(H_1 + H_2c)\}\delta_x^2 \\
&\quad + \{K_2 - 0.5(y_\mathrm{f} - y_\mathrm{b})(K_1 + K_2d)\}\delta_y^2]\delta_t^+\phi_{ij}^n \\
&\quad + [-A_{ij}\delta_x^2 - B_{ij}\delta_y^2 + C_{ij}\delta_x + D_{ij}\delta_y + G_{ij}\delta_x\delta_y - H_{ij}\delta_x\delta_y^2 - K_{ij}\delta_x^2\delta_y - L_{ij}\delta_x^2\delta_y^2]\phi_{ij}^n \\
&\qquad = F_{ij},
\end{aligned} \tag{19}$$

where δ_t^+ denotes the forward difference operator for time with uniform time step Δt and n represents the time level; the coefficients A_{ij} ,B_{ij}, C_{ij}, D_{ij}, G_{ij}, H_{ij}, K_{ij}, L_{ij} and F_{ij} are to be evaluated at the nth time level now.

We now introduce a weighted average parameter μ through the approximation of the time derivative $\partial\phi/\partial t$ such that $t_\mu = (1-\mu)t^{(n)} + \mu t^{(n+1)}$ where $0 \leqslant \mu \leqslant 1$. Varying μ yields different schemes of different time accuracies. For $\mu = 0$, the computational stencil requires nine points at the nth and five points at $(n+1)$th time level resulting in what may be termed as a (9, 5) scheme. Similarly $\mu = 0.5$ and $\mu = 1$ yields a (9, 9) (see the corresponding stencil in Fig. 1) and a (5, 9) scheme, respectively. The temporal order of accuracy is two for the (9, 9) scheme and one for the other two. Note that the corner points appear in the finite difference stencils because of the presence of the finite difference operators $\delta_x\delta_y$, $\delta_x\delta_y^2$, $\delta_x^2\delta_y$ and $\delta_x^2\delta_y^2$ in Eq. (19). With these, Eq. (19) can be put in the form

$$\begin{aligned}
\sum_{k_1=-1}^{1}\sum_{k_2=-1}^{1} w_{i+k_1,j+k_2}\phi_{i+k_1,j+k_2}^{(n+1)} &= \sum_{k_1=-1}^{1}\sum_{k_2=-1}^{1} w'_{i+k_1,j+k_2}\phi_{i+k_1,j+k_2}^{(n)} \\
&\quad + (\mu F_{ij}^{(n+1)} + (1-\mu)F_{ij}^{(n)})\Delta t,
\end{aligned} \tag{20}$$

where $w_{i+k_1,j+k_2} = -\mu\,\Delta t p_{i+k_1,j+k_2} + q_{i+k_1,j+k_2}$ and $w'_{i+k_1,j+k_2} = (1-\mu)\,\Delta t p_{i+k_1,j+k_2} + q_{i+k_1,j+k_2}$ with

$$p_{i-1,j-1} = -\frac{G_{ij}}{4hk} - \frac{H_{ij}}{2hky_\mathrm{b}} - \frac{K_{ij}}{2hkx_\mathrm{b}} + \frac{L_{ij}}{hkx_\mathrm{b}y_\mathrm{b}},$$

$$p_{i-1,j+1} = \frac{G_{ij}}{4hk} - \frac{H_{ij}}{2hky_\mathrm{f}} + \frac{K_{ij}}{2hkx_\mathrm{b}} + \frac{L_{ij}}{hkx_\mathrm{b}y_\mathrm{f}},$$

$$p_{i+1,j-1} = \frac{G_{ij}}{4hk} + \frac{H_{ij}}{2hky_\mathrm{b}} - \frac{K_{ij}}{2hkx_\mathrm{f}} + \frac{L_{ij}}{hkx_\mathrm{f}y_\mathrm{b}},$$

$$p_{i+1,j+1} = -\frac{G_{ij}}{4hk} + \frac{H_{ij}}{2hky_{\mathrm{f}}} + \frac{K_{ij}}{2hkx_{\mathrm{f}}} + \frac{L_{ij}}{hkx_{\mathrm{f}}y_{\mathrm{f}}},$$

$$p_{i,j-1} = \frac{B_{ij}}{ky_{\mathrm{b}}} + \frac{D_{ij}}{2k} + \frac{K_{ij}}{2hk}\left(\frac{1}{x_{\mathrm{f}}} + \frac{1}{x_{\mathrm{b}}}\right) - \frac{L_{ij}}{hk}\left(\frac{1}{x_{\mathrm{f}}y_{\mathrm{b}}} + \frac{1}{x_{\mathrm{b}}y_{\mathrm{b}}}\right),$$

$$p_{i,j+1} = \frac{B_{ij}}{ky_{\mathrm{f}}} - \frac{D_{ij}}{2k} - \frac{K_{ij}}{2hk}\left(\frac{1}{x_{\mathrm{f}}} + \frac{1}{x_{\mathrm{b}}}\right) - \frac{L_{ij}}{hk}\left(\frac{1}{x_{\mathrm{b}}y_{\mathrm{f}}} + \frac{1}{x_{\mathrm{f}}y_{\mathrm{f}}}\right),$$

$$p_{i-1,j} = \frac{A_{ij}}{hx_{\mathrm{b}}} + \frac{C_{ij}}{2h} + \frac{H_{ij}}{2hk}\left(\frac{1}{y_{\mathrm{f}}} + \frac{1}{y_{\mathrm{b}}}\right) - \frac{L_{ij}}{hk}\left(\frac{1}{x_{\mathrm{b}}y_{\mathrm{f}}} + \frac{1}{x_{\mathrm{b}}y_{\mathrm{b}}}\right),$$

$$p_{i+1,j} = \frac{A_{ij}}{hx_{\mathrm{f}}} - \frac{C_{ij}}{2h} + \frac{H_{ij}}{2hk}\left(\frac{1}{y_{\mathrm{f}}} + \frac{1}{y_{\mathrm{b}}}\right) - \frac{L_{ij}}{hk}\left(\frac{1}{x_{\mathrm{f}}y_{\mathrm{b}}} + \frac{1}{x_{\mathrm{f}}y_{\mathrm{f}}}\right),$$

$$p_{ij} = -\frac{A_{ij}}{h}\left(\frac{1}{x_{\mathrm{f}}} + \frac{1}{x_{\mathrm{b}}}\right) - \frac{B_{ij}}{k}\left(\frac{1}{y_{\mathrm{f}}} + \frac{1}{y_{\mathrm{b}}}\right) + \frac{L_{ij}}{hk}\left(\frac{1}{x_{\mathrm{f}}y_{\mathrm{f}}} + \frac{1}{x_{\mathrm{f}}y_{\mathrm{b}}} + \frac{1}{x_{\mathrm{b}}y_{\mathrm{f}}} + \frac{1}{x_{\mathrm{b}}y_{\mathrm{b}}}\right),$$

$$q_{i-1,j-1} = 0,$$

$$q_{i-1,j+1} = 0,$$

$$q_{i+1,j-1} = 0,$$

$$q_{i+1,j+1} = 0,$$

$$q_{i,j-1} = -\frac{b}{2k}(K_1 + K_2 d) + \frac{b}{ky_{\mathrm{b}}}\{K_2 - 0.5(K_1 + K_2 d)(y_{\mathrm{f}} - y_{\mathrm{b}})\},$$

$$q_{i,j+1} = \frac{b}{2k}(K_1 + K_2 d) + \frac{b}{ky_{\mathrm{f}}}\{K_2 - 0.5(K_1 + K_2 d)(y_{\mathrm{f}} - y_{\mathrm{b}})\},$$

$$q_{i-1,j} = -\frac{b}{2h}(H_1 + H_2 c) + \frac{b}{hx_{\mathrm{b}}}\{H_2 - 0.5(H_1 + H_2 c)(x_{\mathrm{f}} - x_{\mathrm{b}})\},$$

$$q_{i+1,j} = \frac{b}{2h}(H_1 + H_2 c) + \frac{b}{hx_{\mathrm{f}}}\{H_2 - 0.5(H_1 + H_2 c)(x_{\mathrm{f}} - x_{\mathrm{b}})\}$$

and

$$q_{ij} = b - \frac{b}{h}\left(\frac{1}{x_{\mathrm{f}}} + \frac{1}{x_{\mathrm{b}}}\right)\{H_2 - 0.5(H_1 + H_2 c)(x_{\mathrm{f}} - x_{\mathrm{b}})\} - \frac{b}{k}\left(\frac{1}{y_{\mathrm{f}}} + \frac{1}{y_{\mathrm{b}}}\right)\{K_2 - 0.5(K_1 + K_2 d)(y_{\mathrm{f}} - y_{\mathrm{b}})\},$$

where $h = (x_{\mathrm{f}} + x_{\mathrm{b}})/2$ and $k = (y_{\mathrm{f}} + y_{\mathrm{b}})/2$. Thus Eq. (20) becomes the HOC finite difference approximation for the 2D unsteady convection–diffusion on nonuniform spatial grids. The point-wise spatial accuracy of the scheme which depends upon the adjacent grid spacing is at least three; it becomes four when uniform space grid is used [15]. Higher spatial accuracy on uniform grid, however, is not an indication of the overall computational efficiency. For example, for the lid-driven cavity flow problem (see Section 4.2), the scheme of Ref. [14] on a 41×41 uniform spatial grid cannot resolve the secondary and tertiary vortices accurately; on the other hand, the same can be achieved on a nonuniform grid of same size with clustering near boundaries using the present scheme.

3. Solution of algebraic systems

We now discuss the solution of algebraic systems associated with the newly proposed finite difference approximations. The system of Eq. (20) can be written in the matrix form as

$$A\boldsymbol{\Phi}^{\mathbf{n+1}} = \mathbf{f}(\boldsymbol{\Phi}^{\mathbf{n}}), \tag{21}$$

where the coefficient matrix A is an asymmetric sparse matrix. For a grid of size $m \times n$, A has a dimension mn, and $\boldsymbol{\Phi}^{\mathbf{n+1}}$ and $\mathbf{f}(\boldsymbol{\Phi}^{\mathbf{n}})$ are mn-component vectors.

The next step now is to solve Eq. (21) with iterative methods. As the coefficient matrix A is not generally diagonally dominant, conventional iterative methods such as Gauss–Seidel cannot be used. On uniform grids, some of the associated matrices are symmetric and positive definite, which allows algorithms like conjugate gradient (CG) [16,24] to be used. As nonuniform grid invariably leads to nonsymmetric matrices, in order to solve these systems the biconjugate gradient stabilized method (BiCGStab) [16,22,24,28] is used here without preconditioning.

To solve the N–S equations using the proposed scheme, we have used the ψ–ω formulations (4)–(6) and employed an outer–inner iteration procedure. In a typical outer temporal cycle, we solve Eq. (4) which is discretized using (20) with $b = Re$, $c = Re\,u$, $d = Re\,v$ and $f = 0$. Then we discretize (5) using (9) with $c = d = 0$ and $f = -\omega$. For both the vorticity and streamfunction equation, BiCGStab [16,22,24] is used, which constitutes the inner iterations. Once (5) is solved, u and v are calculated using a fourth-order compact formula (see Ref. [13]) for (6). This constitutes one outer iteration cycle. We utilize a relaxation parameter γ for the inner iteration cycles for both ω and ψ. For larger values of Reynolds number, we needed smaller values of γ.

All of our computations were carried out on a Pentium 4 based PC with 512 MB RAM. For the inner iterations, the computations were stopped when the maximum ϕ-error (ϕ being either ω or ψ) between two successive iteration steps was smaller than 0.5×10^{-6}. For the time-marching steady-state solution of the lid-driven cavity problem, steady state was assumed to reach when the maximum ω-error between two successive outer temporal iteration steps was smaller than 0.5×10^{-7}. Throughout our computations, we have used the (9, 9) scheme which is unconditionally stable on uniform grids [14].

4. Numerical experiments

In order to study the validity and effectiveness of the proposed scheme, it is applied to two unsteady 2D problems. These are (i) the Taylor vortex problem and (ii) the lid-driven square cavity flow problem. As the first problem has analytical solutions, Dirichlet boundary conditions are used, while for the cavity problem, both Dirichlet (for ψ) and Neumann (for ω) boundary conditions are applied. For the first problem, we use exact initial data whereas for the cavity problem, zero initial data were used in all the computations.

4.1. Test problem 1: the Taylor vortex problem

First we consider the Taylor vortex problem [6,14] governed by Eqs. (1)–(3) in the square $0 \leqslant x, y \leqslant 2\pi$ with the following initial conditions:

$$u(x, y, 0) = -\cos(x)\sin(y) \quad \text{and} \quad v(x, y, 0) = \sin(x)\cos(y). \tag{22}$$

The exact solution of this problem is given by

$$u(x, y, t) = -\cos(x)\sin(y)\mathrm{e}^{-2t/Re} \quad \text{and} \quad v(x, y, t) = \sin(x)\cos(y)\mathrm{e}^{-2t/Re}. \tag{23}$$

The initial and boundary conditions for the ψ–ω formulations (4)–(6) can be easily derived from the exact solution.

As the flow is characterized by a number of free shear layers, in order to resolve the flow accurately, we have generated the grid in such a way (see Fig. 2(a)) that maximum number of points gets allocated to those regions. To generate the grid we have used the following stretching functions:

$$x_i = \frac{\pi}{2}\left\{\frac{i}{i_{\max}} + \frac{\lambda}{\pi}\sin\left(\frac{\pi i}{i_{\max}}\right)\right\} \quad \text{in } 0 \leqslant x, y \leqslant \frac{\pi}{2},$$

$$x_i = \pi\left\{\frac{i}{i_{\max}} - \frac{\lambda}{2\pi}\sin\left(\frac{2\pi i}{i_{\max}}\right)\right\} \quad \text{in } \frac{\pi}{2} \leqslant x, y \leqslant \frac{3\pi}{2},$$

and

$$x_i = \frac{\pi}{2}\left\{\frac{i}{i_{\max}} - \frac{\lambda}{\pi}\sin\left(\frac{\pi i}{i_{\max}}\right)\right\} \quad \text{in } \frac{3\pi}{2} \leqslant x, y \leqslant 2\pi.$$

Here, the parameter λ determines the degree of clustering with greater value of λ indicating more number of grid points at specified locations. For example, the first expression gradually increases point density toward right; the second one

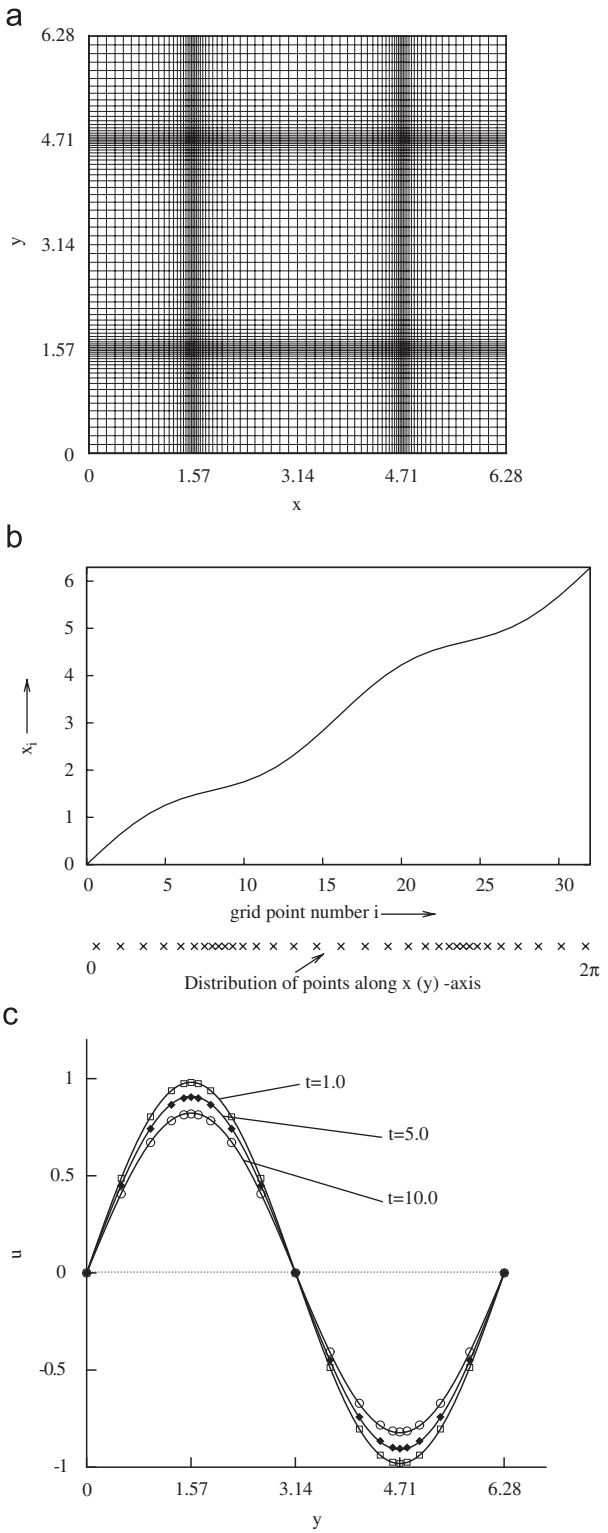

Fig. 2. For the Taylor vortex problem, (a) the 81×81 nonuniform grid, (b) the stretching function as a function of grid points and (c) comparison of the analytical (solid lines) and numerical (symbols) u-velocity along the vertical centerline at time stations $t = 1.0$, 5.0 and 10.0.

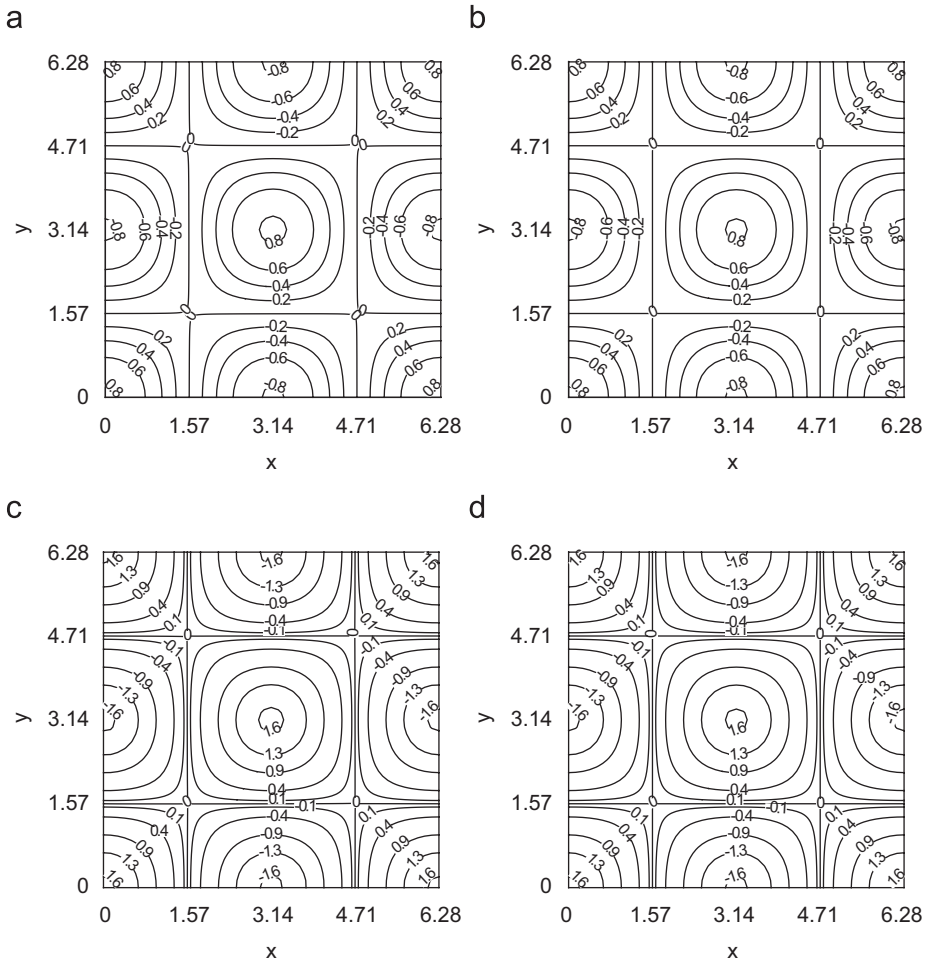

Fig. 3. For the Taylor vortex problem, streamfunction contours: (a) numerical, (b) analytical and vorticity contours: (c) numerical, (d) analytical; all at $t = 10.0$.

generates a centro-symmetric distribution of points with clustering at both the ends whereas the third one gradually increases point density toward left. Throughout our computation including the next problem that follows, we have taken $\lambda = 0.6$ except when stated otherwise. The graph of i versus x_i shown in Fig. 2(b) clearly shows that the grid used here is smooth enough to preserve the order of accuracy.

We present our results computed on a 81×81 grid with $\Delta t = 0.01$ for $Re = 100$ in Figs. 2 and 3. The numerical u-values along the vertical centerline at three different time stations are compared with the exact values in Fig. 2(c). It is clear from the graph that our numerical results show an excellent match with the exact ones, thus exemplifying the ability of the scheme to capture transient solutions accurately. In Fig. 3(a) and (b), we show the numerical and analytical streamlines and Fig. 3(c) and (d) show the corresponding vorticity contours at time $t = 10.0$ for the same Reynolds number. All these figures indicate a very close match of the numerical solution to the exact one including excellent resolution of the shear layers. We notice that the u-velocity along the vertical centerline and the v-velocity along the horizontal centerline are symmetric and have the same maximum amplitude. Therefore, taking this maximum velocity, we define a percentage error as in [6] as

$$\left| \frac{u_{\text{exact}} - u_{\text{numerical}}}{u_{\text{exact}}} \right| \times 100\%.$$

Table 1
Percentage error of the maximum u-velocity at $t = 10$ for $Re = 20$ and 100 ($\Delta t = 0.01$) with the convergence rate

Re	Grid	Present (uniform)	Rate	Present ($\lambda = 0.6$)	Rate
20	33×33	0.1100249%		0.2608062%	
			3.995		3.932
	65×65	0.0069021%		0.0170834%	
		(0.206%)	3.982		3.978
	129×129	0.0004367%		0.0010844%	
		(0.038%)			
100	33×33	0.880100%		1.70520%	
			3.983		3.700
	65×65	0.005567%		0.013121%	
			4.004		3.963
	129×129	0.000348%		0.0008414%	

We now present this error for $Re = 20$ and 100 with $\Delta t = 0.01$ and compare the one for $Re = 20$ with that of [6] (values given within parentheses) in Table 1. It is obvious from the table that our numerical results are superior to them and the error decays with $O(h^4)$ as expected.

4.2. Test problem 2: the lid-driven square cavity problem

Next we consider the 2D lid-driven square cavity problem. This problem, over the years, has become the most frequently used benchmark problem for the assessment of numerical methods, particularly the steady-state solution of the incompressible fluid flows governed by the N–S [1,3–5,7,11,14,15,17,23,29]. This problem is of great scientific interest because it displays almost all fluid mechanical phenomena for incompressible viscous flows in the simplest of geometric settings. The cavity is defined as the square $0 \leqslant x, y \leqslant 1$. The fluid motion is generated by the sliding motion of the top wall of the cavity ($y = 1$) in its own plane from left to right. This moving wall generates vorticity which diffuses inside the cavity and this diffusion is the driving mechanism of the flow. At high Re, several secondary and tertiary vortices begin to appear, whose characteristics depend on Re. Because of the presence of large gradients near the walls, while generating the computational grid, care was taken so that there were enough points in the vicinity of the boundary so as to meet the criteria $\delta \sim Re^{-0.5}$ and $h^* \sim Re^{-0.75}$, where δ, h^* are the (nondimensional) boundary layer thickness and distance between the wall and the first point closest to it [2,21,27]. To generate a centro-symmetric grid with clustering near the walls, we use the stretching function

$$x_i = \frac{i}{i_{\max}} - \frac{\lambda}{2\pi} \sin\left(\frac{2\pi i}{i_{\max}}\right), \quad 0 < \lambda \leqslant 1$$

in both x- and y-directions.

4.2.1. HOC wall boundary conditions

Boundary conditions for velocity on the top wall are given by $u = 1$, $v = 0$. On all other walls of the cavity the velocities are zero ($u = v = 0$). In the ψ–ω setting used here, streamfunction values on all the four walls are zero ($\psi = 0$).

We now proceed to develop transient HOC wall boundary conditions for vorticity ω in the following manner:

At the left wall, where the index for x-direction is 0 and j is the y-direction index varying from 0 to $y_{\max}$, on using forward difference, we have

$$v_{0j} = -\left.\frac{\partial \psi}{\partial x}\right|_{0j} = -\delta_x \psi_{0j} + \frac{x_f}{2}\left.\frac{\partial^2 \psi}{\partial x^2}\right|_{0j} + \frac{x_f^2}{6}\left.\frac{\partial^3 \psi}{\partial x^3}\right|_{0j} + \frac{x_f^3}{24}\left.\frac{\partial^4 \psi}{\partial x^4}\right|_{0j} + O(x_f^4).$$

As $v_{0j} = 0$, using Eq. (5), we have

$$0 = -\left[\delta_x^+ \psi + \frac{x_f}{2}\left(\omega + \frac{\partial^2 \psi}{\partial y^2}\right) + \frac{x_f^2}{6}\left(\frac{\partial \omega}{\partial x} + \frac{\partial^3 \psi}{\partial x\, \partial y^2}\right) + \frac{x_f^3}{24}\left(\frac{\partial^2 \omega}{\partial x^2} + \frac{\partial^4 \psi}{\partial x^2\, \partial y^2}\right)\right]_{0j} + O(x_f^4).$$

Also in view of the fact that $\partial^2\psi/\partial y^2 = (\partial/\partial y)(u) = 0$, $(\partial^3\psi/\partial x\,\partial y^2) = \partial^2 v/\partial y^2 = 0$ on the left wall and $\partial^4\psi/\partial x^2\,\partial y^2 = (\partial^3/\partial x\,\partial y^2)(\partial\psi/\partial x) = -\partial^3 v/\partial x\,\partial y^2$ [using (6)], the above relation becomes

$$0 = \left[-\delta_x^+\psi - \frac{x_f}{2}\omega - \frac{x_f^2}{6}\left(\delta_x^+\omega - \frac{x_f}{2}\frac{\partial^2\omega}{\partial x^2}\right) - \frac{x_f^3}{24}\left(\frac{\partial^2\omega}{\partial x^2} - \frac{\partial^3 v}{\partial x\,\partial y^2}\right)\right]_{0j} + O(x_f^4). \tag{24}$$

Making use of the fact that the velocities are constant (0 or 1) on the walls, Eq. (4) yields $Re(\partial\omega/\partial t) - \nabla^2\omega = 0$. Using this to replace $\partial^2\omega/\partial x^2$ in (24), the following fourth-order accurate approximation is obtained on the left wall:

$$\delta_t^+\omega_{0j} = \frac{1}{Re}\left[\frac{24}{x_f^3}\delta_x^+\psi + \frac{12}{x_f^2}\omega + \frac{4}{x_f}\delta_x^+\omega + \delta_y^2\omega - \delta_x^+\delta_y^2 v\right]_{0j}. \tag{25}$$

Boundary conditions for ω on the other three walls can be derived in a similar way.

4.2.2. Results and discussions

Computations were carried out for this problem for the range of Re's 100–5000 on grids of sizes ranging from 21×21 to 121×121.

In Fig. 4, we present comparisons of the steady-state horizontal velocities on the vertical centerline and the vertical velocities on the horizontal centerline of the square cavity for Reynolds numbers ranging from 100 to 5000 and compare

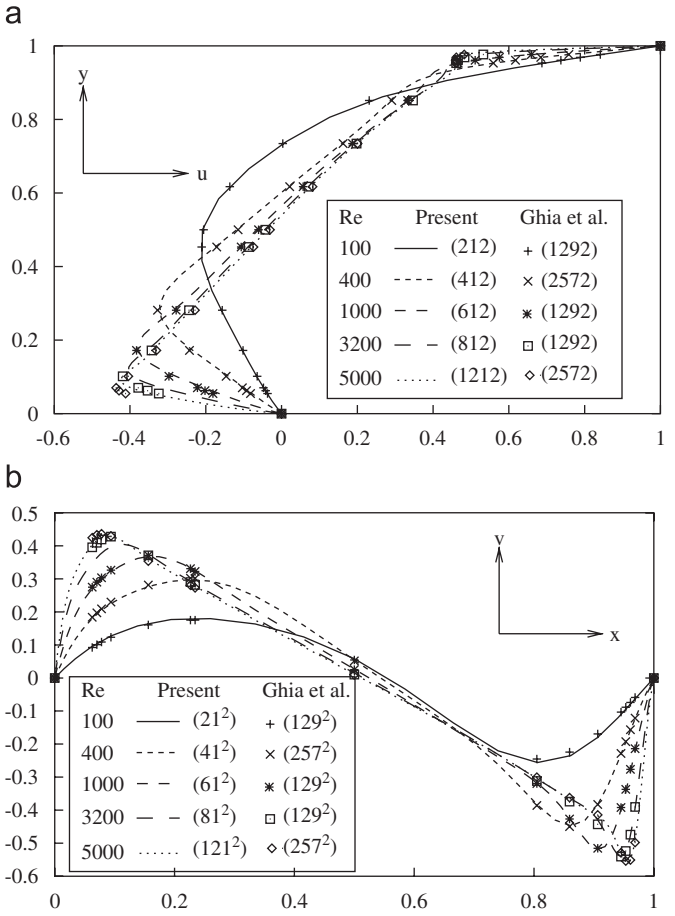

Fig. 4. Comparisons of steady-state (a) horizontal velocity along the vertical centerline and (b) vertical velocity along the horizontal centerline for the lid-driven square cavity flow problem from $Re = 100$ to 5000.

Table 2
Properties of steady-state primary, secondary and tertiary vortices for the lid-driven square cavity from $Re = 100$ to 5000

Vortex	Property	Re				
		100	400	1000	3200	5000
Primary	$\psi_{\min}$	−0.103	−0.112	−0.117	−0.117	−0.119
		(−0.103)	(−0.114)	(−0.118)	(−0.120)	(−0.119)
	Location x, y	0.5844, 0.7400	0.5424, 0.6253	0.5282, 0.5567	0.5212, 0.5424	0.5142, 0.5424
		(0.6172, 0.7344)	(0.5547, 0.6055)	(0.5313, 0.5625)	(0.5165, 0.5469)	(0.5117, 0.5352)
Secondary	$\psi_{\max}$	–	–	–	4.57e − 4	1.21e − 3
Top left		–	–	–	(7.28e − 4)	(1.46e − 3)
	Location x, y	–	–	–	0.0462, 0.8958	0.0599, 0.9057
		–	–	–	(0.0547, 0.8984)	(0.0625, 0.9125)
	H_{L}	–	–	–	0.0772	0.1139
		–	–	–	(0.0859)	(0.1211)
	V_{L}	–	–	–	0.2054	0.2683
		–	–	–	(0.2057)	(0.2693)
Bottom left	$\psi_{\max}$	1.82e − 6	1.32e − 5	2.10e − 4	8.44e − 4	1.13e − 3
		(1.75e − 6)	(1.42e − 5)	(2.31e − 4)	(9.78e − 4)	(1.36e − 3)
	Location x, y	0.0343, 0.0340	0.0462, 0.0462	0.0816, 0.0816	0.0846, 0.1149	0.0757, 0.1304
		(0.0313, 0.0391)	(0.0508, 0.0469)	(0.0859, 0.0781)	(0.0859, 0.1094)	(0.0703, 0.1367)
	H_{L}	0.0678	0.1214	0.2191	0.2950	0.3217
		(0.0781)	(0.1273)	(0.2188)	(0.2844)	(0.3184)
	V_{L}	0.0670	0.1033	0.1665	0.2402	0.2704
		(0.0781)	(0.1081)	(0.1680)	(0.2305)	(0.2643)
Bottom right	$\psi_{\max}$	1.22e − 5	6.19e − 4	1.72e − 3	2.85e − 3	3.11e − 3
		(1.25e − 5)	(6.42e − 4)	(1.75e − 3)	(3.14e − 3)	(3.08e − 3)
	Location x, y	0.9401, 0.0599	0.8850, 0.1150	0.8614, 0.1077	0.8208, 0.0939	0.7957, 0.0757
		(0.9453, 0.0625)	(0.8906, 0.1250)	(0.8594, 0.1094)	(0.8125, 0.0859)	(0.8086, 0.0742)
	H_{L}	0.1378	0.2598	0.3062	0.3730	0.3871
		(0.1328)	(0.2617)	(0.3034)	(0.3406)	(0.3565)
	V_{L}	0.1384	0.3338	0.3607	0.4149	0.4422
		(0.1484)	(0.3203)	(0.3536)	(0.4102)	(0.4180)
Tertiary	$\psi_{\min}$	–	–	−4.64e − 9	−1.84e − 8	−4.60e − 8
Bottom left		–	–	–	(−2.52e − 7)	(−7.08e − 8)
	Location x, y	–	–	0.0050, 0.0050	0.0038, 0.0076	0.0076, 0.0076
		–	–	–	(0.0078, 0.0078)	(0.0117, 0.0078)
	H_{L}	–	–	0.0101	0.0152	0.0157
		–	–	–	(0.0254)	(0.0156)
	V_{L}	–	–	0.0101	0.0158	0.0161
		–	–	–	(0.0234)	(0.0163)
Tertiary	$\psi_{\min}$	–	−1.40e − 8	−3.73e − 8	−2.05e − 7	−1.48e − 6
Bottom right		–	(−1.86e − 8)	(−9.32e − 8)	(−2.52e − 7)	(−1.46e − 6)
	Location x, y	–	0.9924, 0.0076	0.9950, 0.0102	0.9885, 0.0115	0.9787, 0.0213
			(0.9922, 0.0078)	(0.9922, 0.0078)	(0.9844, 0.0078)	(0.9805, 0.0195)
	H_{L}	–	0.0156	0.0156	0.0262	0.0569
		–	(0.0156)	(0.0078)	(0.0254)	(0.0528)
	V_{L}	–	0.0156	0.0157	0.0250	0.0446
		–	(0.0156)	(0.0078)	(0.0234)	(0.0417)
Grid size		21 × 21	41 × 41	61 × 61	81 × 81	121 × 121
		(129 × 129)	(257 × 257)	(129 × 129)	(129 × 129)	(257 × 257)

our data with those of Ghia et al. [7]. While the data for [7] was obtained using 129 × 129 and 257 × 257 grids, our data are obtained using a 21 × 21 grid ($Re = 100$), a 41 × 41 grid ($Re = 400$), a 61 × 61 grid ($Re = 1000$), a 81 × 81 grid ($Re = 3200$) and a 121 × 121 grid ($Re = 5000$). In each case, our velocity profiles exhibit a perfect match with Ghia's results.

In Table 2, we provide the quantitative comparison data for our solutions. Here we present the steady-state primary, secondary and tertiary vortex center data for $100 \leqslant Re \leqslant 5000$ and compare them with those of Ghia et al. [7] (values

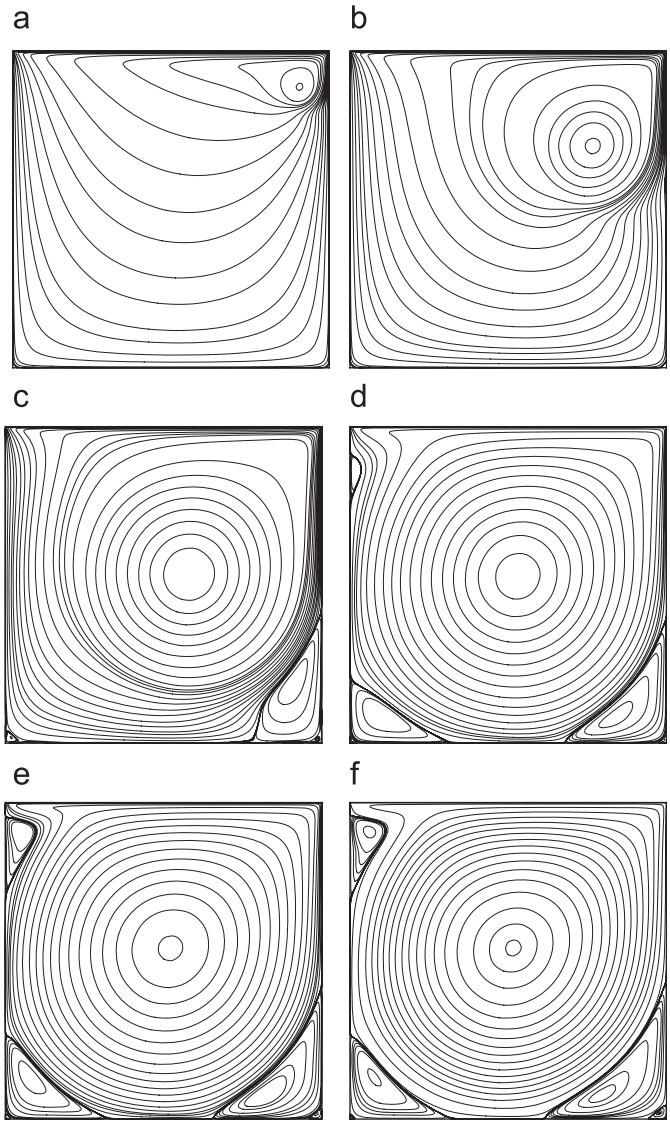

Fig. 5. Streamlines contours for the lid-driven cavity flow for $Re = 5000$ at $t =$ (a) 5, (b) 20, (c) 60, (d) 100, (e) 160 and (f) 1500.

given within parentheses). Our results again exhibit an excellent match with this as well as other published results [1,3–5,11,14,15,17,23,29].

In Fig. 5, we show the timewise evolution of the streamlines at $Re = 5000$ till the steady-state is reached (on a 121×121 grid). These figures show that our scheme excellently captures the formation of the secondary and tertiary vortices as time progresses. Fig. 6 shows the convergence history of the vorticity residuals for $Re = 100$ and 1000 captured with $\Delta t = 0.01$ on various grid sizes. Here we have defined the residual as $\|\omega^{(n+1)} - \omega^{(n)}\|_2 / \|\omega^{(n+1)}\|_2$, where n and $n+1$ denote successive time-levels and $\|.\|_2$ is the l_2 norm. The residual was allowed to fall below 5×10^{-11} in order to eliminate the oscillations. Expectedly, our experiments with lowering the tolerance limit below this value did not result in any significant change in our computations. The CPU times taken were 5.294 and 48.460 s, respectively, on 21×21 and 41×41 grids for $Re = 100$ and, 23.412 and 129.368 s on the same grids for $Re = 1000$.

The explicit versus implicit issue has always been a moot point among the computational fluid dynamics community. While a stable solution for time-dependent problem is possible with implicit schemes with larger time steps, it is also a point of concern as it may lead to an increase in the truncation error. Therefore, temporal order of accuracy may become

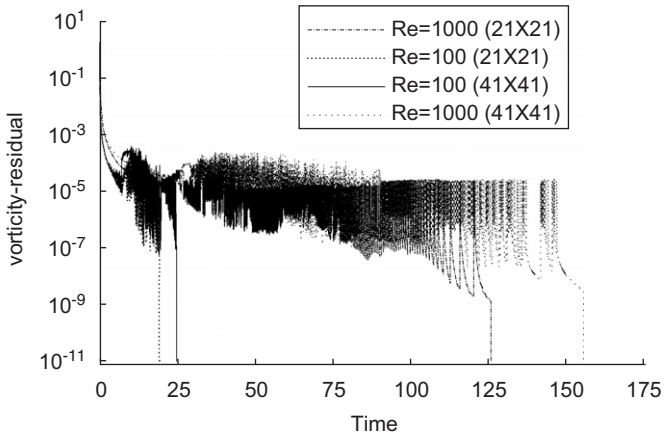

Fig. 6. Convergence history of the ω-residuals for the lid-driven cavity flow for $Re = 100$ and 1000.

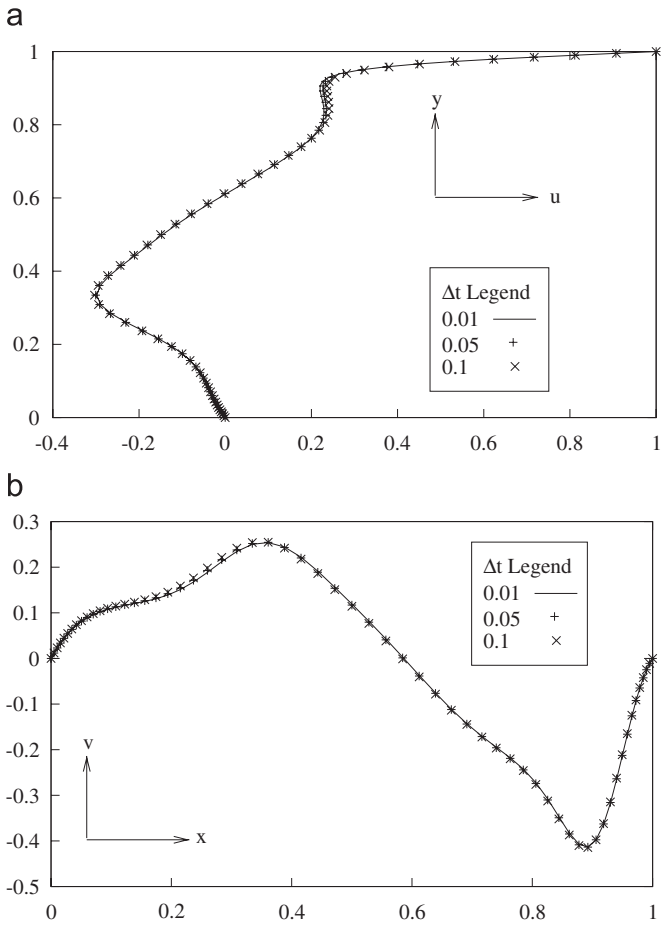

Fig. 7. (a) Horizontal velocity along the vertical centerline and (b) vertical velocity along the horizontal centerline for the lid-driven square cavity problem for $Re = 1000$ at $t = 20.0$ captured with $\Delta t = 0.1$, 0.05 and 0.01.

an important factor in capturing time-accurate solutions. To examine the effects of time steps in the numerical solution, we plotted the horizontal velocity along the vertical centerline and vertical velocity along the horizontal centerline (in Fig. 7(a) and (b), respectively) at instant $t = 20.0$ captured with three different time steps $\Delta t = 0.1$, 0.05 and 0.01

for $Re = 1000$. Overlapping of the profiles clearly indicates that second-order temporal accuracy is good enough to produce time-accurate solutions with a relatively larger time step of $\Delta t = 0.1$ in the present case.

5. Conclusions

In this paper, we develop an implicit HOC scheme for the unsteady 2D N–S equations on nonuniform space grids. Locally, the scheme is second-order accurate in time and third or fourth-order accurate in space depending upon the pattern of grid spacing. Both Dirichlet and Neumann boundary conditions can easily be incorporated into the scheme. It is easy to implement and the use of BiCGStab algorithm for solving the algebraic systems arising at every time level makes the implicit procedure computationally efficient even in capturing transient solutions. To bring out different aspects of the scheme, we employed it to compute the transient solutions of the Taylor vortex problem and the time marching steady solution of the 2D lid-driven cavity flow problem. The robustness of the scheme is illustrated by its applicability to problems of varying physical complexities, represented among others, by Reynolds numbers ranging from 100 to 5000. The results obtained in both the test cases with relatively coarser grids are in excellent agreement with the analytical as well as established numerical results, underlining the high accuracy of the scheme. The implicit nature of the scheme is fully exploited in arriving at the steady-state results for the lid-driven cavity problem, where time-steps as high as 0.1 have been employed for some of the computations. As the scheme has the added advantages of nonuniformity of grids with simplicity (no grid transformation), and resolution of mixed scales typical of free shear layer (Taylor vortex problem), and wall bounded shear layer (lid-driven cavity problem), it has a good potential for efficient application to many problems of incompressible viscous flows. Currently we are working on the application of the scheme to curvilinear coordinates.

Appendix A. Details of the finite difference operators

The expressions for the finite difference operators appearing in Eq. (19) are as follows:

$$\delta_x \phi_{ij} = \frac{\phi_{i+1,j} - \phi_{i-1,j}}{2h}, \tag{26}$$

$$\delta_y \phi_{ij} = \frac{\phi_{i,j+1} - \phi_{i,j-1}}{2k}, \tag{27}$$

$$\delta_x^2 \phi_{ij} = \frac{1}{h}\left\{\frac{\phi_{i+1,j}}{x_\mathrm{f}} - \left(\frac{1}{x_\mathrm{f}} + \frac{1}{x_\mathrm{b}}\right)\phi_{ij} + \frac{\phi_{i-1,j}}{x_\mathrm{b}}\right\}, \tag{28}$$

$$\delta_y^2 \phi_{ij} = \frac{1}{k}\left\{\frac{\phi_{i,j+1}}{y_\mathrm{f}} - \left(\frac{1}{y_\mathrm{f}} + \frac{1}{y_\mathrm{b}}\right)\phi_{ij} + \frac{\phi_{i,j-1}}{y_\mathrm{b}}\right\}, \tag{29}$$

$$\delta_x \delta_y \phi_{ij} = \frac{1}{4hk}(\phi_{i+1,j+1} - \phi_{i+1,j-1} - \phi_{i-1,j+1} + \phi_{i-1,j-1}), \tag{30}$$

$$\begin{aligned}\delta_x \delta_y^2 \phi_{ij} = \frac{1}{2hk}\Bigg\{&\frac{1}{y_\mathrm{f}}(\phi_{i+1,j+1} - \phi_{i-1,j+1}) - \left(\frac{1}{y_\mathrm{f}} + \frac{1}{y_\mathrm{b}}\right)(\phi_{i+1,j} - \phi_{i-1,j}) \\ &+ \frac{1}{y_\mathrm{b}}(\phi_{i+1,j-1} - \phi_{i-1,j-1})\Bigg\},\end{aligned} \tag{31}$$

$$\begin{aligned}\delta_x^2 \delta_y \phi_{ij} = \frac{1}{2hk}\Bigg\{&\frac{1}{x_\mathrm{f}}(\phi_{i+1,j+1} - \phi_{i+1,j-1}) - \left(\frac{1}{x_\mathrm{f}} + \frac{1}{x_\mathrm{b}}\right)(\phi_{i,j+1} - \phi_{i,j-1}) \\ &+ \frac{1}{x_\mathrm{b}}(\phi_{i-1,j+1} - \phi_{i-1,j-1})\Bigg\},\end{aligned} \tag{32}$$

$$\delta_x^2\delta_y^2\phi_{ij} = \frac{1}{hk}\left\{\frac{\phi_{i+1,j+1}}{x_{\mathrm{f}}y_{\mathrm{f}}} + \frac{\phi_{i-1,j+1}}{x_{\mathrm{b}}y_{\mathrm{f}}} - \left(\frac{1}{x_{\mathrm{f}}y_{\mathrm{f}}} + \frac{1}{x_{\mathrm{b}}y_{\mathrm{f}}}\right)\phi_{i,j+1} - \left(\frac{1}{x_{\mathrm{f}}y_{\mathrm{f}}} + \frac{1}{x_{\mathrm{f}}y_{\mathrm{b}}}\right)\phi_{i+1,j} + \left(\frac{1}{x_{\mathrm{f}}y_{\mathrm{f}}} + \frac{1}{x_{\mathrm{f}}y_{\mathrm{b}}} + \frac{1}{x_{\mathrm{b}}y_{\mathrm{f}}} + \frac{1}{x_{\mathrm{b}}y_{\mathrm{b}}}\right)\phi_{ij} - \left(\frac{1}{x_{\mathrm{f}}y_{\mathrm{b}}} + \frac{1}{x_{\mathrm{b}}y_{\mathrm{b}}}\right)\phi_{i,j-1} - \left(\frac{1}{x_{\mathrm{b}}y_{\mathrm{f}}} + \frac{1}{x_{\mathrm{b}}y_{\mathrm{b}}}\right)\phi_{i-1,j} + \frac{\phi_{i+1,j-1}}{x_{\mathrm{f}}y_{\mathrm{b}}} + \frac{\phi_{i-1,j-1}}{x_{\mathrm{b}}y_{\mathrm{b}}}\right\}. \tag{33}$$

References

[1] E. Barragy, G.F. Carey, Stream function-vorticity driven cavity solution using p finite elements, Comput. Fluids 26 (1997) 453–468.
[2] G.K. Batchelor, An Introduction to Fluid Dynamics, Cambridge University Press, Cambridge, 1974.
[3] M. Ben-Artzi, J.-P. Croisille, D. Fishelov, S. Trachtenberg, A pure-compact scheme for the streamfunction formulation of Navier–Stokes equations, J. Comput. Phys. 205 (2) (2005) 640–664.
[4] O. Botella, R. Peyret, Benchmark spectral results on the lid-driven cavity flow, Comput. Fluids 27 (1998) 421–433.
[5] C.-H. Bruneau, C. Jouron, An efficient scheme for solving steady incompressible Navier–Stokes equations, J. Comput. Phys. 89 (1990) 389–413.
[6] Y.-N. Chen, S.-C. Yang, J.-Y. Yang, Implicit weighted essentially non-oscillatory schemes for the incompressible Navier–Stokes equations, Int. J. Numer. Methods Fluids 31 (1999) 747–765.
[7] U. Ghia, K.N. Ghia, C.T. Shin, High re-solution for incompressible Navier–Stokes equation and a multigrid method, J. Comput. Phys. 48 (1982) 387–411.
[8] M.M. Gupta, High accuracy solutions of incompressible Navier–Stokes equations, J. Comput. Phys. 93 (1991) 343–357.
[9] M.M. Gupta, J.C. Kalita, A new paradigm for solving Navier–Stokes equations: streamfunction-velocity formulation, J. Comput. Phys. 207 (1) (2005) 52–68.
[10] M.M. Gupta, R.M. Manohar, J.H. Stephenson, A single cell high order scheme for the convection–diffusion equation with variable coefficients, Int. J. Numer. Methods Fluids 4 (1984) 641–651.
[11] S. Hou, Q. Zou, S. Chen, G. Doolen, A. Cogley, Simulation of cavity flows by the lattice boltzmann method, J. Comput. Phys. 118 (1995) 329–347.
[12] J.C. Kalita, P. Chhabra, An improved (9,5) higher order compact scheme for the transient two-dimensional convection–diffusion equation, Int. J. Numer. Methods Fluids 51 (2006) 703–717.
[13] J.C. Kalita, D.C. Dalal, A.K. Dass, Fully compact higher order computation of steady-state natural convection in a square cavity, Phys. Rev. E 64 (6) (2001) 066703 (1–13).
[14] J.C. Kalita, D.C. Dalal, A.K. Dass, A class of higher order compact schemes for the unsteady two-dimensional convection–diffusion equation with variable convection coefficients, Int. J. Numer. Methods Fluids 38 (2002) 1111–1131.
[15] J.C. Kalita, A.K. Dass, D.C. Dalal, A transformation-free HOC for steady convection–diffusion on nonuniform grids, Int. J. Numer. Methods Fluids 44 (2004) 33–53.
[16] C.T. Kelley, Iterative Methods for Linear and Nonlinear Equations, SIAM, Philadelphia, 1995.
[17] J. Kim, P. Moin, Application of fractional step method to incompressible Navier–Stokes equation, J. Comput. Phys. 59 (1985) 308–323.
[18] S.K. Lele, Compact finite difference schemes with spectral like resolution, J. Comput. Phys. 103 (1992) 16–42.
[19] M. Li, T. Tang, B. Fornberg, A compact fourth order finite difference scheme for the steady incompressible Navier–Stokes equations, Int. J. Numer. Methods Fluids 20 (1995) 1137–1151.
[20] R.J. Mackinnon, R.W. Johnson, Differential equation based representation of truncation errors for accurate numerical solution, Int. J. Numer. Methods Fluids 13 (1991) 739–757.
[21] M. Nallasamy, K.K. Prasad, On cavity flows at high Reynolds numbers, J. Fluid Mech. 79 (1977) 391–414.
[22] Y. Saad, Iterative Methods for Sparse Linear Systems, PWS, Boston, 1996.
[23] R. Schreiber, H.B. Keller, Driven cavity flows by efficient numerical techniques, J. Comput. Phys. 49 (1983) 310–333.
[24] G.L.G. Sleijpen, H.A. van der Vorst, Hybrid biconjugate methods for CFD problems, in: M. Hafez, K. Oshima (Eds.), Computational Fluid Dynamics Review, 1995, pp. 457–476.
[25] W.F. Spotz, G.F. Carey, High-order compact scheme for the steady stream-function vorticity equations, Int. J. Numer. Methods Eng. 38 (1995) 3497–3512.
[26] J.C. Strikwerda, High-order accurate schemes for incompressible viscous flow, Int. J. Numer. Methods Fluids 24 (1997) 715–734.
[27] S. Sundaresan, Clustered grids and mesh-independence in numerical simulation of 2-D lid-driven cavity flows, Ph.D. Thesis, Department of Aerospace Engineering, Indian Institute of Science, Bangalore, India, 1995.
[28] H. van der Vorst, BiCGSTAB: a fast and smoothly converging variant of BiCG for the solution of nonsymmetric linear systems, SIAM J. Sci. Comput. 13 (1992) 631–644.
[29] S.P. Vanka, Block-implicit multigrid solution of Navier–Stokes equations in primitive variables, J. Comput. Phys. 65 (1986) 138–158.